machines

MDPI

Article

Research on GIS Circuit Breaker Fault Diagnosis Based on Closing Transient Vibration Signals

Yue Yu and Hongyan Zhao *

College of Mechanical & Energy Engineering, Beijing University of Technology, Beijing 100124, China; yybjut28@163.com
* Correspondence: zhaohy@bjut.edu.cn

Abstract: GIS circuit breakers play a critical role in maintaining the reliability of modern power systems. However, mechanical failures, such as spring fatigue, transmission rod jamming, and loosening of structural components, can significantly impact their performance. Traditional diagnostic methods struggle to identify these issues effectively due to the enclosed nature of GIS equipment. This study explores the use of vibration signal analysis, specifically during the closing transient phase of the GIS circuit breaker. The proposed method combines wavelet packet decomposition, rough set theory for feature extraction and dimensionality reduction, and the S_Kohonen neural network for fault type identification. Experimental results demonstrate the robustness and accuracy of the method, achieving a diagnostic accuracy of 96.7% in identifying mechanical faults. Compared with traditional methods, this approach offers improved efficiency and accuracy in diagnosing GIS circuit breaker faults. The proposed method is highly applicable for predictive maintenance and fault diagnosis in power grid systems, contributing to enhanced operational safety and reliability.

Keywords: GIS (gas-insulated switchgear); fault diagnosis; vibration signal analysis; wavelet packet transform; S_Kohonen neural network

check for updates

Academic Editor: Hui Ma

Received: 28 February 2025
Revised: 5 April 2025
Accepted: 8 April 2025
Published: 18 April 2025

Citation: Yu, Y.; Zhao, H. Research on GIS Circuit Breaker Fault Diagnosis Based on Closing Transient Vibration Signals. *Machines* **2025**, *13*, 335. https://doi.org/10.3390/machines13040335

Copyright: © 2025 by the authors. Licensee MDPI, Basel, Switzerland. This article is an open access article distributed under the terms and conditions of the Creative Commons Attribution (CC BY) license (https://creativecommons.org/licenses/by/4.0/).

1. Introduction

With the continuous development of power systems, especially to meet the demands of ultra-high voltage (UHV) power transmission, gas-insulated metal-enclosed switchgear (GIS) has become a critical high-voltage electrical equipment. In recent years, GIS fault diagnosis has attracted widespread attention, with researchers conducting in-depth explorations from multiple perspectives. Regarding fault types, GIS equipment failures primarily include mechanical faults and electrical faults [1]. Mechanical issues related to circuit breakers constitute a major portion of GIS faults, such as operating mechanism failures, external solid insulation deterioration, and transient voltage faults [2]. Metal debris causing electric field distortion and air gap breakdown under electric field forces is also identified as a significant cause of insulation breakdown in 220 kV GIS circuit breakers [3].

Concerning diagnostic methods, ultra-high frequency and ultra-sonic techniques are widely employed to detect internal defects in GIS [4], with comprehensive diagnosis and localization being achieved through the combined application of ultra-high frequency, ultra-sonic, SF_6 gas composition analysis, and X-ray imaging technologies [5]. Vibration signal analysis, as an important non-electrical detection method, effectively diagnoses GIS mechanical defects by analyzing signal amplitude, spectrum, and waveform distortion [6], particularly under large-current variable-frequency excitation conditions, which allow for

more precise simulation and detection of mechanical defects [7]. Long-term monitoring of GIS equipment's mechanical vibration signals helps establish defect development models and predict defect trends [8], while sound signal processing technology, especially the Mel-frequency cepstral coefficients (MFCCs) method, has also proven effective in distinguishing different types of mechanical faults [9].

Signal processing technology is a key component of GIS fault diagnosis. Researchers employ various advanced algorithms to process vibration and sound signals, including wavelet packet decomposition [10], ensemble empirical mode decomposition (EEMD) [11], and S-transform [12]. By analyzing the time–domain and frequency–domain characteristics of GIS circuit breaker vibration signals and their relationships with fault types, feature parameters characterizing electrical contact faults can be extracted [13].

Artificial intelligence technology is increasingly applied in GIS fault diagnosis. Various intelligent algorithms are used for GIS fault identification, such as BP neural networks [14], improved sparrow search algorithm-optimized BP neural networks [15], convolutional neural networks (CNNs) [16], and deep belief networks (DBNs) [17]. Some studies convert vibration signal sequences into vibration images, establishing mechanical fault detection models based on convolutional neural networks (VI-CNNs) [18], while others enhance the extraction capability of partial discharge features by improving convolutional neural networks through attention mechanisms and enhanced pooling layers [19]. Research on deep learning applications in medium-voltage switchgear fault detection indicates that different algorithms have their respective advantages and applicable scenarios in partial discharge diagnosis [20].

Although CNN and LSTM algorithms have shown promising results in GIS fault diagnosis, they have several limitations in practical applications. CNN-based methods require extensive preprocessing of vibration signals and large datasets for training, which can be computationally intensive and time-consuming [16]. LSTM networks, while effective at capturing temporal dependencies in sequential data, often face challenges with convergence speed and are sensitive to parameter initialization [21]. In contrast, our proposed approach combining wavelet packet transform with rough set theory and S_Kohonen network offers significant advantages in terms of computational efficiency, training data requirements, and robustness to noise.

Multi-feature fusion technology has significantly improved the accuracy and reliability of GIS fault diagnosis. Methods based on multi-source feature dual-decision hybrid classification networks effectively improve the classification accuracy of similar faults by analyzing various signals from control motors [22]. The combination of multi-source data with convolutional neural networks [23] has been proven effective in identifying different types and complexities of GIS faults.

For GIS disconnector fault diagnosis, researchers have analyzed common fault types and their causes, constructing effective fault diagnosis models based on multiple signals [24]. Some researchers have built 126 kV GIS mechanical fault testing systems, proposing energy-equalized S-transform (EE-ST) methods to extract fault features [25], achieving effective diagnosis of GIS circuit breaker mechanical faults.

Overall, while GIS fault diagnosis technology has made significant progress, it still faces numerous challenges. Current research primarily focuses on identifying single or limited types of faults, lacking comprehensive diagnostic capabilities for multiple and complex faults. Additionally, interference factors in actual operating environments, optimization of sensor placement, and reliability assessment of diagnostic results require further investigation. Therefore, this paper proposes a fault diagnosis method based on GIS circuit breaker closing transient vibration signals, combining wavelet packet transform for feature extraction and rough set theory for dimensionality reduction, while employing

the S_Kohonen network for fault pattern classification. By analyzing vibration signal characteristics during the GIS circuit breaker closing process, this method effectively identifies mechanical faults such as transmission rod jamming, spring fatigue loosening, and drive crank arm screw loosening, achieving a diagnostic accuracy of 96.7%. Compared with traditional methods, the proposed approach demonstrates significant improvements in diagnostic efficiency and accuracy, providing reliable support for GIS circuit breaker fault warning and equipment maintenance, which is of great significance for enhancing power grid operational safety and reliability.

2. GIS Vibration Characteristics Analysis

2.1. Normal Vibration Mechanism Analysis of GIS

The GIS shell is typically designed as a coaxial cylindrical structure to ensure a uniform electric field distribution inside. According to the busbar configuration, the GIS can be classified into two types: three-phase separated structures and three-phase common structures. Below is an analysis of the electrodynamic forces in both configurations.

(1) Three-Phase Separated GIS: The three-phase separated structure is the most prevalent form of GISs. Each phase conductor is housed within its own enclosed cavity. Under normal conditions, when the conductors are energized, the outer shell is assumed to be grounded. The three-phase conductors inside the GIS busbar are arranged parallel to each other and have the same length. As shown in Figure 1, if conductors 1 and 2 are energized, the electrodynamic force on each conductor can be determined.

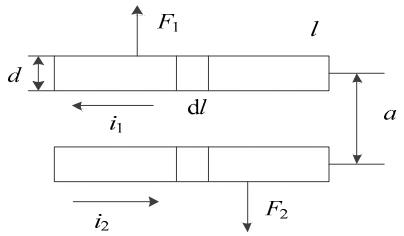


Figure 1. GIS parallel conductor force.

When calculating the induced electromotive force generated by induced current, it is assumed that the magnetic field is uniformly distributed inside the GIS enclosure. The magnetic flux density produced by conductor 2 at the position of conductor 1 is:

$$B_2 = u_0 u_r H_2 = \frac{u_0 u_r i_2}{2\pi a} = \frac{u_0 u_r I_m}{2\pi a} \sin(\omega t - 120^\circ) \tag{1}$$

In Equation (1), $i_2 = I_m \sin(\omega t - 120^\circ)$, $i_1 = I_m \sin(\omega t)$, μ_0 represents the vacuum magnetic permeability, and H_2 refers to the magnetic field intensity produced by conductor 2 at the position of conductor 1.

According to the electromechanical force calculation formula and the integration theorem, the electromechanical force experienced by conductor 1 is:

$$\begin{aligned} F_1 &= \int_0^l B_2 i_1 dl = B_2 i_1 l = \frac{u_0 u_r I_m^2 l}{2\pi a} \sin(\omega t) \sin(\omega t - 120^\circ) \\ &= -\frac{u_0 u_r I_m^2 l}{8\pi a} \left[1 - \cos(2\omega t) + \sqrt{3} \sin(2\omega t)\right] \end{aligned} \tag{2}$$

where i_1 and i_2 are the currents in the two conductors. The electrodynamic force's frequency is twice the power frequency (i.e., $2 \times 50\,\text{Hz} = 100\,\text{Hz}$).

(2) Three-Phase Common GIS: In the three-phase common GIS structure, three-phase conductors are arranged in a common busbar space, with currents through each

phase being mutually displaced by 120°. Taking the A-phase conductor as an example, the current flowing through the A-phase conductor is set as $i_a = I_m \sin(\omega t)$, while $i_b = I_m \sin(\omega t - 120^\circ)$ and $i_c = I_m \sin(\omega t + 120^\circ)$ represent currents in the other phases. Figure 2 illustrates this structural configuration and the magnetic force condition at a specific moment. The central positions of the conductors are denoted by a, b, and c, while B_{ba} and B_{ca} represent the magnetic flux densities at the A-phase generated by B- and C-phases, respectively. The distances between the three-phase conductors are l_{ba}, l_{ca}, and l_{bc}, with $l_{ba} = l_{ca} = l_{bc} = d$.

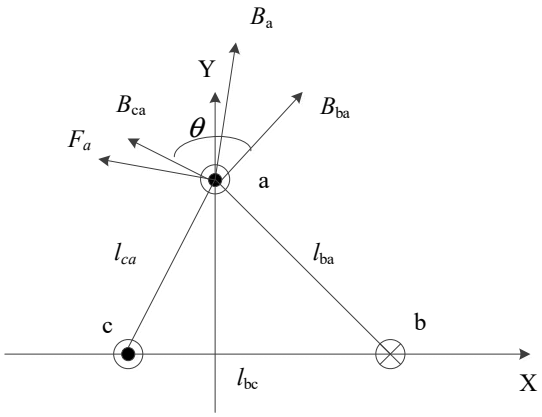


Figure 2. GIS three-phase commons.

According to the magnetic flux density calculation formula, the magnetic flux densities generated by B-phase and C-phase conductors at the position of the A-phase conductor are, respectively:

$$B_{ba} = \frac{u_0 u_r I_m}{2\pi l_{ba}} \sin(\omega t - 120^\circ) \tag{3}$$

$$B_{ca} = \frac{u_0 u_r I_m}{2\pi l_{ca}} \sin(\omega t + 120^\circ) \tag{4}$$

The total magnetic flux density of the A-phase conductor is:

$$B_a = \sqrt{B_{ba}^2 + B_{ca}^2 - 2B_{ba}B_{ca}\cos(180^\circ - \theta)} \tag{5}$$

Therefore, the magnitude of the electromechanical force experienced by the A-phase conductor (with length l) is:

$$F_a = B_a i_a l = \frac{\sqrt{3} u_0 u_r I_m^2 l}{4\pi d} \sin(2\omega t) \tag{6}$$

where I_1 and I_2 denote phase currents separated by 120°. The mutual induction among conductors A, B, and C arises from their respective currents. Notably, the frequency of this electrodynamic force is also twice the power frequency—i.e., 100 Hz.

In summary, whether the GIS design employs a three-phase separated or a three-phase common structure, the system vibrates at a fundamental frequency of 100 Hz as a result of electrodynamic forces.

Magnetostriction refers to slight dimensional changes in magnetic materials under various magnetization states and orientations. Fluctuations in temperature, magnetic fields, and electric fields can lead to changes in a material's dimensions, generating mechanical vibrations. Consequently, the magnetostrictive effect's contribution can be evaluated by monitoring variations in the vibration acceleration of a given material.

Under normal conditions, the thickness of the GIS enclosure can be neglected compared to its radius, so the GIS enclosure can be treated as a thin-shell structure with a

uniform magnetic field distribution inside. Therefore, we can roughly assume that the magnetic field intensity in the enclosure equals that in the thin shell:

$$H = \frac{B}{u_0 u_r} = \frac{B_0 \cos(\omega t)}{u_0 u_r} \tag{7}$$

Before ferromagnetic materials reach magnetic saturation, the effect of magnetostriction appears as a change in length, known as linear magnetostriction. In the thin-shell structure of GIS, the relationship between linear deformation and magnetic field intensity can be expressed by the following equation:

$$|H|\mathrm{d}H = \frac{H_c^2}{2\lambda_s \cdot \delta}\mathrm{d}\delta \tag{8}$$

In Equation (8), H_c represents the coercive force, which actually refers to a magnetic field of a certain magnitude. This magnetic field is opposite to the direction of the original magnetizing field and can reduce the original magnetic field to zero; thus, the coercive force is also called the "coercive field". λ_s represents the saturation magnetostriction coefficient (of the GIS thin shell).

According to the relationship between μ and H, the magnitude of the magnetic field intensity in the GIS thin shell is:

$$H = \frac{B}{u} = \frac{B}{B_s}H_c = \frac{B_0}{B_s}H_c \cos(\omega t) \tag{9}$$

In the above equation, B_s represents the saturation magnetic flux density, $B_s = \frac{u_r^2}{2\pi R}$. Combining Equation (9), the calculation result for the magnetostriction coefficient λ of the GIS enclosure is:

$$\lambda = \frac{\Delta\delta}{\delta} = \frac{2\lambda_s}{H_c^2}\int_0^H |H| dH = \frac{\lambda_s}{H_c^2}H^2 = \frac{\lambda_s u_0^2 I_0^2}{2\pi R B_s}\cos^2(\omega t) \tag{10}$$

Hence, the magnetostrictive acceleration of the GIS shell can be described by:

$$a = \frac{d^2(\Delta\delta)}{dt^2} = -\frac{2w^2\lambda_s\delta u_0^2 I_0^2}{\pi R B_s^2}\cos(2\omega t)$$

where α is a proportionality constant and λ is the magnetostrictive coefficient. As a result, the magnetostrictive vibration typically shares the same frequency—100 Hz—as the electrodynamic force. Therefore, during normal operation, both electrodynamic and magnetostrictive effects excite the GIS shell at 100 Hz (twice the fundamental power frequency of 50 Hz).

2.2. GIS Circuit Breaker Operating Mechanism Force and Energy Analysis

Within a GIS, the circuit breaker is one of its most critical components, and its vibration properties are a central focus in research. Key parameters for GIS circuit breakers include rated voltage, rated current, rated interrupting current, thermal stability current, closing time, and auto-reclosing performance. Notably, the circuit breaker's opening and closing actions produce vibration signatures containing valuable diagnostic information. These operations are rapid, frequent, and instantaneous, with distinct vibration behavior for different conditions. Because the operating mechanism represents a substantial portion of mechanical faults, understanding how forces and energy evolve within the mechanism is essential for analyzing vibration signals. The vibration fault frequency spectra signatures are primarily influenced by several GIS characteristics, including electrodynamic forces, magnetostrictive effects, and the mechanical properties of the operating mechanism:

(1) Electrodynamic Forces: The forces exerted by the current in the busbar and conductor system influence the vibration frequencies. The configuration of the GIS components, such as conductor spacing and arrangement, can also affect these forces.

(2) Magnetostrictive Effects: Changes in the magnetic field strength within GIS components, due to the flow of current, result in magnetostrictive forces that contribute to the vibration spectra.

(3) Mechanical Components: The mechanical operation of the circuit breaker, including the spring system and transmission components (e.g., rods, link arms), generates characteristic vibration frequencies. Mechanical wear, fatigue, and fault development (such as spring loosening or transmission rod jamming) lead to changes in these spectra, often resulting in shifts in frequency or increased amplitude at specific frequencies.

The vibration spectra can change over time due to several factors:

(1) Fault Development: As faults such as spring fatigue or mechanical jamming progress, the frequency spectra will show variations in the amplitude of specific frequency components, indicating the nature of the fault.

(2) Operational Stress: Prolonged operation and mechanical wear affect the response of the GIS components, leading to shifts or changes in the vibration characteristics.

(3) Environmental Effects: Variations in environmental conditions such as temperature or humidity can affect the material properties and vibration behavior of GIS components, causing subtle changes in the fault frequency spectra.

2.2.1. Force Analysis of GIS Circuit Breaker Operating Mechanism

As outlined in Figure 3, the GIS circuit breaker operating mechanism comprises multiple subsystems: an energy storage system, a control system, and a transmission system. An energy storage motor and mechanism accumulate energy, which is subsequently released by the control assembly to actuate the spring for opening and closing operations. The cushioning device guards the operating mechanism, while force, motion, and the stored spring energy are conveyed to the breaker's contacts through a transmission assembly, thus governing their motion.

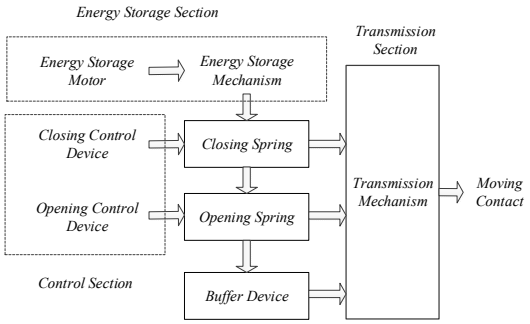


Figure 3. Block diagram of GIS circuit breaker actuating mechanism structure.

The GIS circuit breaker operating mechanism undergoes several stages during its operation, including the closing process, contact collision, and subsequent wear and fatigue of mechanical components. Each of these stages can give rise to faults that manifest as changes in the vibration signals, including spring fatigue, transmission rod jamming, and loose link arms. These faults may occur gradually and often begin with subtle changes in vibration characteristics.

The impact of inherent fault stages on the proposed fault diagnosis scheme is significant, particularly in the early stages of fault development. For example, spring fatigue may initially result in only slight changes in vibration amplitude, which could be difficult to detect using standard methods. Similarly, minor transmission rod jamming may not imme-

diately cause a dramatic shift in the frequency spectra, leading to potential misclassification if the fault is not identified at an early stage.

To address these challenges, the proposed scheme utilizes a combination of advanced signal processing techniques, including wavelet packet decomposition, feature extraction, and rough set theory for dimensionality reduction. These methods enhance the sensitivity of the model to small, gradual changes in vibration patterns, which improves the ability to detect early-stage faults. Furthermore, the S_Kohonen network is trained to classify faults based on subtle shifts in the frequency spectra, allowing for the detection of faults even as they develop over time.

During the closing operation, the main driving force is the spring force; gravitational effects are generally negligible. The closing process can be divided into two stages: (i) before the dynamic and static contacts collide; and (ii) after they collide.

Before contact collision: the total load force on the breaker during closing can be approximated as:

$$F = F_{\mathrm{e}} + F_t + F_f \tag{11}$$

After contact collision: once the moving and static contacts collide, the forces acting on the mechanism change. The load force is then:

$$F' = F_z + F_e + F_t + F_f + F_d + F_h \tag{12}$$

During opening/closing cycles, the spring force is particularly significant, comprising contributions from the opening spring, closing spring, and the contact springs. The spring force can be expressed as:

$$F_a = F_0 - C\frac{\mathrm{d}l}{\mathrm{d}t} + k(l_0 - l) \tag{13}$$

where k is the spring constant and l is the spring's compression or extension from its equilibrium length.

2.2.2. Energy Analysis of GIS Circuit Breaker Actuator Closing State

As depicted in Figure 4, throughout the closing operation, the closing spring's energy originates from the energy storage motor and mechanism. Upon receiving a closing command, the closing spring releases its stored energy through the transmission mechanism, transferring it to the discharge spring and the moving contact. This energy transfer completes the closing operation; however, a certain portion of energy is inevitably lost due to friction or other inefficiencies within the transmission path.

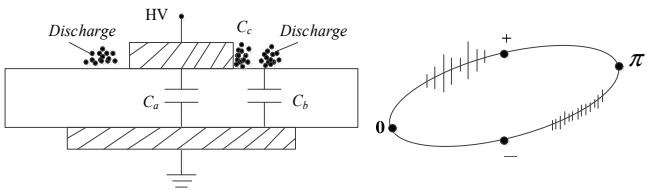


Figure 4. Insulator discharge along the surface.

The energy relationship of the closing spring is:

$$W_{hz} = E_{fz} + W_{ct} + E_f \tag{14}$$

The energy received by the dynamic contact is used to maintain contact pressure and provide kinetic energy for work:

$$W_{ct} = E_{dc} + E_p \tag{15}$$

Based on the definition and calculation formula for work, the energy stored by the closing spring is related to the spring stiffness and deformation and can be expressed as:

$$W_{hz} = \frac{1}{2}k(\Delta l^2 - \Delta l_0^2) \tag{16}$$

3. Experimental Study of GIS Fault Diagnosis

3.1. Experimental Platform Setup

The GIS experimental gap and the dimensions of each structure are shown in Figure 5. All experiments were carried out in a controlled high-voltage laboratory to minimize external disturbances. The ambient temperature within the lab was maintained at approximately 25 °C, and basic electromagnetic shielding was employed to reduce potential interference from external electrical equipment. Additionally, the test bench was placed on a vibration-isolated platform to mitigate any low-frequency mechanical noise transmitted through the floor. These measures ensured a stable and repeatable testing environment for accurately measuring vibration signals under different fault conditions. The overall experimental structure is L-shaped, consisting of three independent chambers and one T-shaped structure. All GIS insulation fault experiments are conducted within a linear cavity.

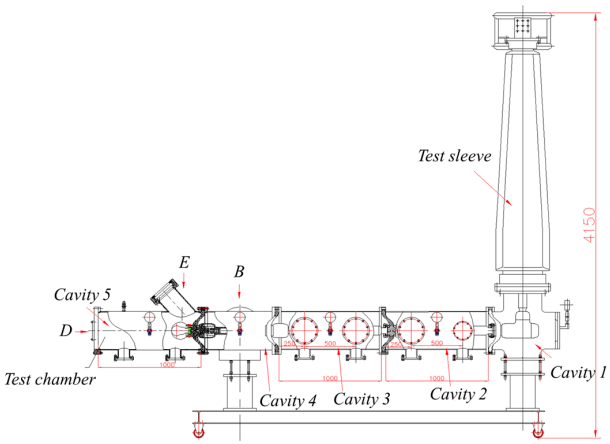


Figure 5. GIS test bay diagram.

Figure 6 presents the physical diagram of the GIS equipment in the high-voltage laboratory. The experimental gap is a three-phase split-type, connected to the experimental voltage through high-voltage bushings.



Figure 6. Photograph of the 220 kV GIS equipment.

Because the operating mechanism is a common fault-prone part of GIS circuit breakers, this study focuses on this structure. To obtain comprehensive vibration signals from the operating mechanism, six vibration sensors from 1# to 6#, are installed at various positions of GIS structure on its surface, as shown in Figure 7. The sensor layout considers different angles and directions to ensure the comprehensiveness of the data. To facilitate observation and simulate faults, the side panel of the operating mechanism is removed, ensuring consistency and comparability across different states.

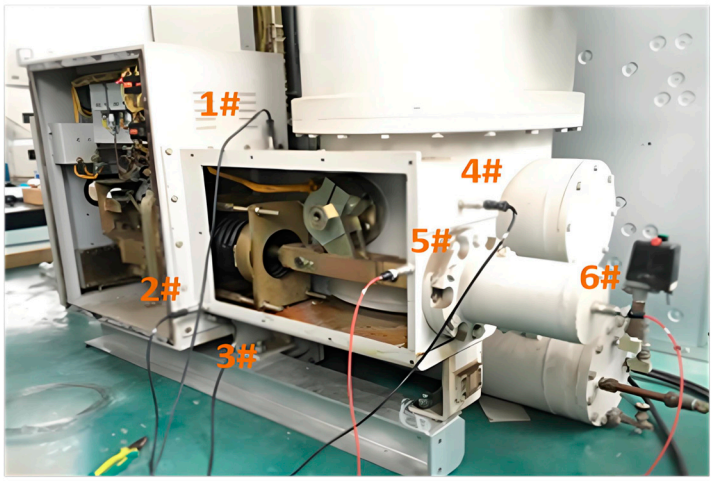


Figure 7. Diagram of sensor placement in the operating mechanism.

The measurement circuit for the GIS circuit breaker operating mechanism consists of the experimental GIS circuit breaker, vibration sensors, conditioning circuits, data acquisition instruments, and industrial control computers, as shown in Figure 8.

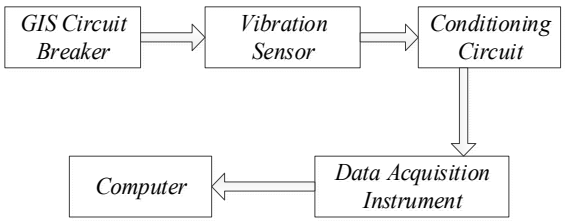


Figure 8. Flowchart of the operating mechanism's measurement circuit.

The vibration measurement units in the experiment include vibration sensors and data acquisition instruments. Before conducting any fault simulations, each AC102-1A vibration sensor underwent a calibration process to verify its accuracy and consistency. We compared the sensor readings against a reference accelerometer under a controlled vibration source at key frequency ranges (e.g., 50 Hz, 100 Hz, and 200 Hz). The calibration confirmed that the sensitivity of each sensor remained within $\pm 1\%$ of the nominal 100 mV/g specification (Figure 9). The parameters of the sensor are listed in Table 1. During each trial, the NICOLET 7700 data acquisition system recorded vibration signals at a 16 kHz sampling rate over a 12 s time window. This sampling frequency was chosen to fully capture both transient and steady-state components of the vibration (Figure 10), which is used to process the vibration signals acquired from the sensors. The vibration data were acquired at a sampling frequency of 16 kHz, ensuring that the relevant frequency components of the vibration signal were captured with sufficient resolution. This sampling rate was chosen based on the Nyquist–Shannon theorem, which guarantees accurate representation of the vibration signal within the bandwidth of the sensor. The sensor used in this experiment has a bandwidth limit of 25,600 Hz, which is much higher than the sampling rate, ensuring

that all relevant vibration frequencies are captured. The acquisition time was set to 12 s to capture both transient and steady-state vibrations during the GIS circuit breaker operation.



Figure 9. Vibration measurement unit.

Table 1. Vibration sensor specifications.

Sensitivity	Repeatability	Range	Resonant Frequency
100 mV/g	1 (%F. S.)	50 g	30 kHz



Figure 10. Nicolet data acquisition instrument.

3.2. GIS Circuit Breaker Typical Faults Artificial Simulation

Among all GIS faults, GIS circuit breaker faults account for a significant proportion, similar to the defects caused by insulator surface discharge, and are among the most common faults. The operating mechanism plays a critical role in GIS circuit breakers, significantly affecting the operational quality of the GIS. Faults such as transmission mechanism jamming and spring fatigue loosening have occurred multiple times. Research shows that vibration signals generated by the same type of equipment are similar, allowing for the analysis of its working condition through the comparison of vibration characteristics from similar devices.

(1) Transmission Rod Jamming

The opening and closing of GIS circuit breakers rely on the transmission rod, and frequent operations may lead to wear or jamming, causing severe failures such as failure to operate or incorrect operation. Therefore, the transmission rod plays a crucial role in the switching process and normal operation of the equipment. In the experiment, black rubber rings were fixed at both ends of the transmission rod. The tension of the rubber rings hinders the rod's normal movement, simulating the transmission rod jamming fault, as shown in Figure 11.

Figure 12 shows rubber rings composed of the same material but with different diameters (37 cm and 43 cm), used to simulate varying degrees of jamming in the transmission rod.

(2) Spring Fatigue Loosening

The energy stored in the spring is the primary power source for the opening and closing operations of the GIS circuit breaker. Repeated operations can cause the spring to experience fatigue and loosening. In the experiment, the fault was simulated by adjusting

the spring's fixing screws, as shown in Figure 13. By varying the position and number of screws, different levels of spring fatigue and loosening were simulated.

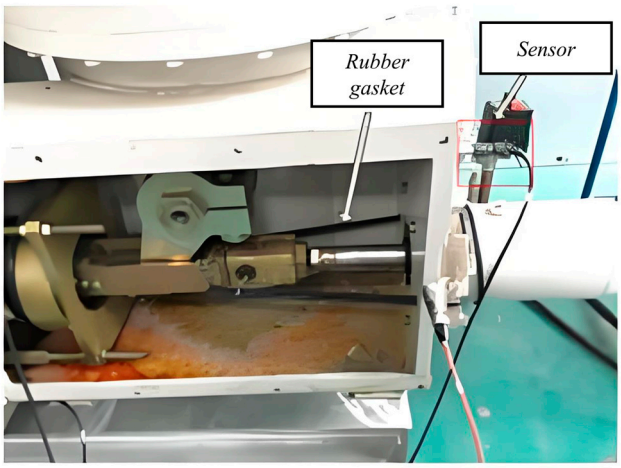


Figure 11. Simulation of transmission rod jamming fault.



Figure 12. Rubber rings of different diameters.

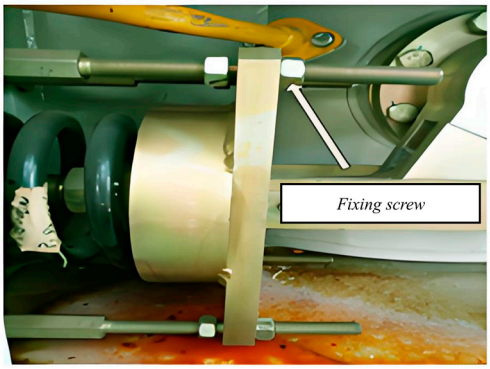


Figure 13. Simulation of spring fatigue and loosening fault.

Two fault states were set in the experiment: a 4 mm and 8 mm loosening of the spring, corresponding to two degrees of spring fatigue loosening.

(3) Transmission Link Arm Screw Loosening

In the GIS circuit breaker's switching process, the transmission link arm connects the spring mechanism to the drive device, transmitting stored spring energy to the drive. The link arm is fixed with screws, and frequent operations can cause these screws to loosen, resulting in poor connection of structural parts and affecting the performance of the operating mechanism.

In the experiment, the fault was simulated by adjusting the loosening of the screws in the transmission link arm, as shown in Figure 14. The degree of loosening was simulated by varying the position and number of loose screws.

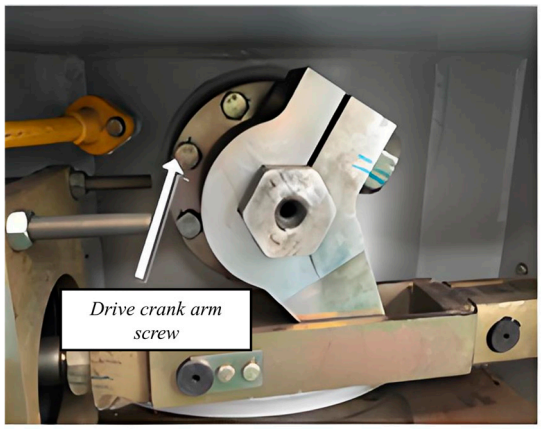


Figure 14. Simulation of drive crank screw loosening fault.

4. GIS Circuit Breaker Fault Study Based on Closing Transient Vibration Signals

This study proposes a fault diagnosis method for GIS circuit breakers based on closing transient vibration signals. Figure 15 illustrates the complete process flow, starting with experimental setup and data acquisition, followed by fault simulation and signal preprocessing, then feature extraction using wavelet packet decomposition, dimensionality reduction through rough set theory, and finally fault classification using the improved S_Kohonen neural network. In the following sections, we will analyze the time–domain waveform characteristics of closing transient vibration signals and explore the vibration properties under different fault conditions.

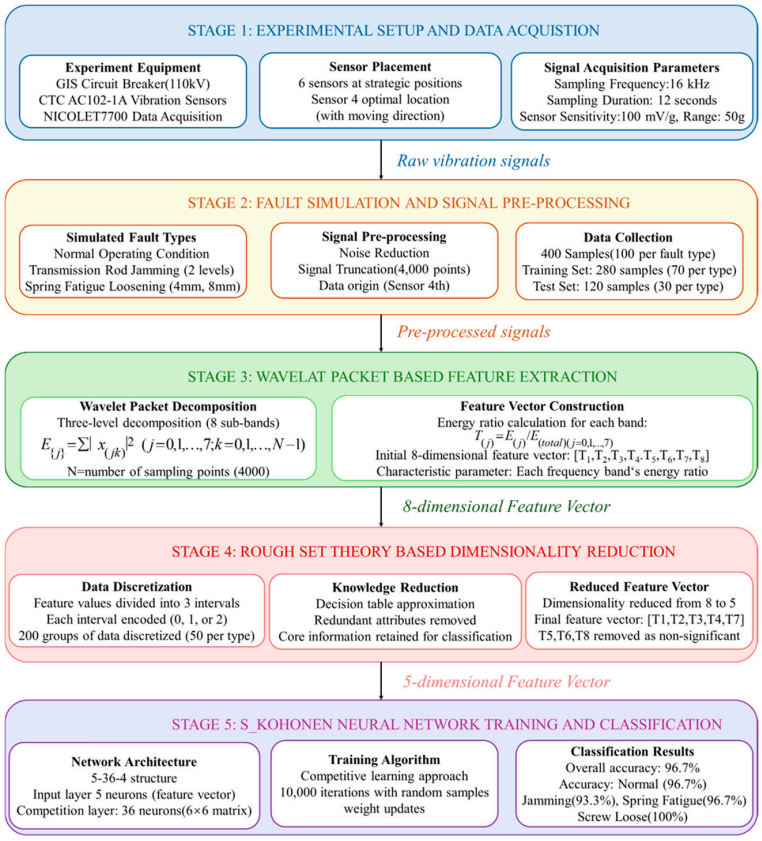


Figure 15. Signal processing pipeline for fault identification in GIS circuit breakers using wavelet-based vibration analysis.

4.1. Time–Domain Waveform Analysis of Closing Transient Vibration Signals

In this experiment, vibration signals from GIS circuit breakers were analyzed in the time domain to identify fault signatures. However, environmental noise can interfere with the detection of these signatures. To ensure the reliability of the fault signatures, several noise reduction techniques were applied during the signal processing phase.

Noise filtering: A low-pass filter was applied to the raw vibration signals to remove high-frequency noise, ensuring that the relevant fault-related frequencies were preserved.

Wavelet denoising: Wavelet-based denoising was employed to smooth the signals and suppress residual noise. This method is particularly effective at reducing non-stationary noise while maintaining the key fault-related features in the signal.

This study selects the GIS circuit breaker with a voltage rating of 110kV as the research object. Due to the influence of the site environment and experimental conditions, closing vibration signals of the GIS circuit breaker in normal operating conditions were measured multiple times for analysis. Figure 16 shows the time–domain waveforms of closing vibration signals measured by six sensors.

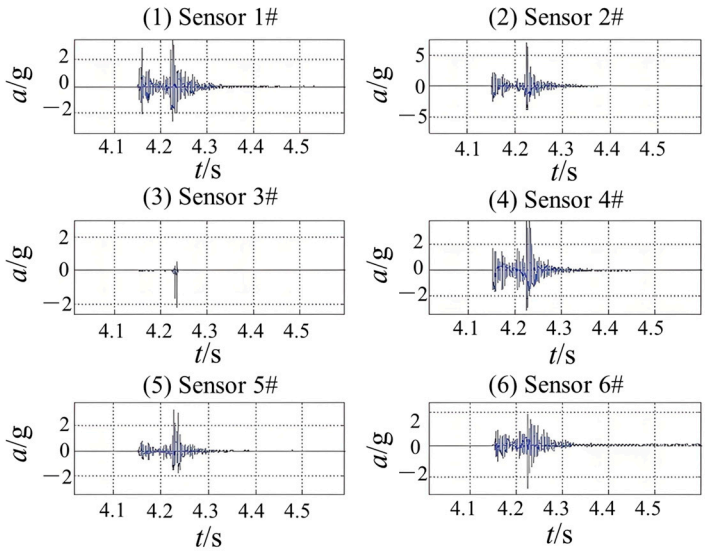


Figure 16. Time–Domain waveforms of closing vibration signals at different measurement points.

The sensor numbering corresponds to the installation positions of the GIS circuit breaker operating mechanism sensors in Section 3. From Figure 16, it can be seen that, compared with the sensors installed at other locations, the closing vibration signal measured by sensor 3 is incorrect and thus discarded. The remaining sensors all successfully measure the closing transient vibration signal of the GIS circuit breaker. At the moment of closing, the amplitude of the vibration signal increases significantly. Sensors 2 and 3 are installed at the base of the operating mechanism, where they are more likely to be influenced by external factors. Sensor 5 is located at the edge of the operating mechanism, with a small contact area with the structural parts, resulting in an unstable signal. Sensor 6 is installed axially at the top of the buffer, where the buffer attenuates the closing transient vibration signal, making it impossible to guarantee the accuracy of the signal. Sensors 1 and 4 are installed on the shell of the operating mechanism, and their measured vibration signals are similar. Sensor 4, whose installation direction aligns with the movement direction of the operating mechanism, is found to most effectively reflect the internal state of the GIS circuit breaker. Therefore, subsequent studies will rely on the signal collected by sensor 4.

During the experimental phase, it is difficult to control the consistency of the closing time and signal collection length. Therefore, the collected signals are first truncated, with a length of 4000 points. Due to the complexity of the field experiment operation, the

vibration signal undergoes basic noise reduction processing. The selected closing transient vibration signals contain various fault types, and their time–domain waveforms are shown in Figure 17.

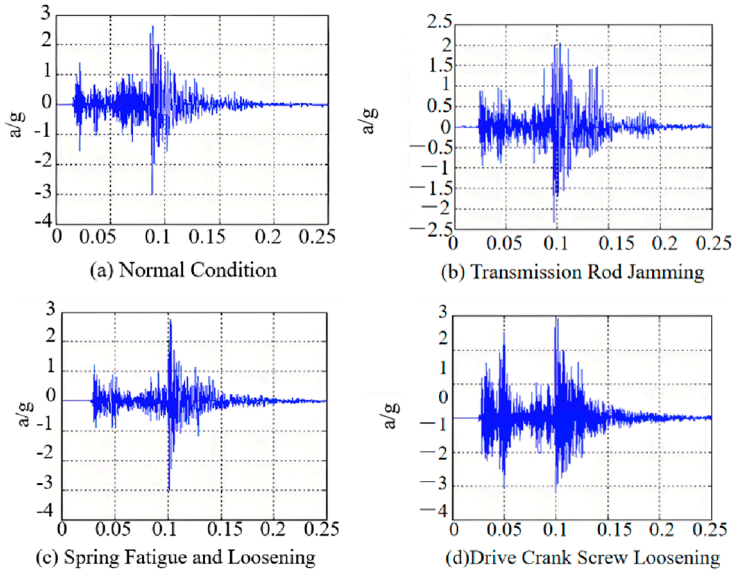


Figure 17. Time–Domain waveforms of transient closing vibration signals under different conditions.

From Figure 17, it can be observed that the closing transient vibration signals under the four conditions differ from one another. In the time–domain waveform, during faults, the amplitude of the vibration signal increases, and the sparsity of the vibration signal over time varies under different fault conditions. Therefore, the vibration characteristics and operational states of the GIS circuit breaker can be identified directly from the closing transient vibration signal waveform. However, the time–domain waveforms alone provide only a qualitative distinction. To more intuitively analyze the operational state of the GIS circuit breaker, feature vectors of the closing transient vibration signals under different conditions need to be extracted.

4.2. Feature Volume Extraction Based on Wavelet Packet and Rough Set Approximation

In this study, signal features were extracted using wavelet packet decomposition with three decomposition levels. This number of levels was chosen after testing different configurations to ensure that the relevant frequency bands were captured without significantly increasing computational complexity.

The three-level decomposition provided a good balance between capturing detailed frequency information and maintaining computational efficiency. The decomposition levels effectively isolated the key fault-related frequency components, which were then used for feature extraction. Increasing the number of decomposition levels beyond three did not yield significant improvements in fault classification accuracy, while also increasing the processing time.

Rough set theory effectively addresses various uncertainty problems. Its minimal expression is derived by ensuring consistent information and removing unnecessary complexity.

$S = (U, A, V, f)$ is a quaternion of a database system, where U denotes the non-empty set of objects; $A = C \cup D$ denotes the non-empty finite set; C is the set of conditional attributes; D is the set of decision attributes; and $C \cap D = \varnothing$; V denotes the attribute value domain. $f : U \times A \rightarrow V$ is the set of relations between U and A. In the fault diagnosis process, the extracted feature information is the conditional attribute and the fault type is the decision attribute.

Knowledge reduction is a key step in rough set theory. It eliminates redundant information while maintaining the essential representation of the database to achieve its minimum form.

Extracting accurate and effective feature vectors is crucial for correct fault diagnosis. Knowledge reduction helps reduce the size of feature information and simplifies the data, improving diagnostic efficiency [26–28]. The steps in knowledge reduction are outlined below:

(1) Removing a conditional attribute from the decision table must be retained if the remaining rules appear to be contradictory;

(2) The kernel value of this conditional attribute is calculated and retained according to Definition 2;

(3) Simplify the rules to obtain the minimum decision table and the reduced feature volume.

The closing transient vibration signal changes quickly. According to the wavelet packet principle, this rapidly changing signal can be broken down into different frequency bands, with the decomposition varying across scales. Additionally, both high and low frequencies can be effectively decomposed, with better separation of the high-frequency components.

Wavelet packet decomposition can be accomplished using different criteria, such as thresholding, decomposition levels, or wavelet base selection. The result from the energy method is called the wavelet packet energy spectrum, which is the main focus of this study. The closing vibration signal of the GIS circuit breaker changes with its operating state. These changes affect the signal's time, peak value, and amplitude. As a result, the energy distribution across frequency bands will shift with the circuit breaker's state. Thus, the wavelet packet decomposition can effectively reflect the GIS circuit breaker's operating condition.

The vibration signal is subjected to a three-layer wavelet packet decomposition, with $E_3(i)$ representing the energy of each node in the third layer and $W(3,i)$ representing the signal at each node in the third layer [29,30]. Then:

$$E_3(i) = \int |W(3,i)|^2 \mathrm{d}t = \sum_{k=1}^{N} |x_{ik}|^2 \tag{17}$$

In this equation, x_{ik} represents the value of each discrete point of the signa $E_3(i)$; N is the number of sampling points. $i = 0, 1, 2, \cdots, 7$ and $k = 1, 2, \cdots, N$.

According to the calculation results of Equations (1)–(5), the characteristic parameter T is constructed:

$$T = [E_3(0)/S_3, \cdots, E_3(7)/S_3] \tag{18}$$

which are denoted by $T_0, T_1, T_2, \cdots, T_7$, where S_3 is the total energy of the third layer of the wavelet packet decomposition of the vibration signal in three layers.

This study analyzes vibration signals measured multiple times under different operating conditions. A three-level wavelet packet decomposition is then applied. The average energy distribution for each frequency band is calculated. The results are shown as a bar chart for comparison. Each state's average is based on five measurements, as shown in Figure 18. As shown in Figure 18, after wavelet packet decomposition, the energy distribution across the third-level bands changes significantly under different states. When faults occur, such as transmission rod jamming, spring fatigue, or loosening of drive arm bolts, the energy in each frequency band also changes accordingly, reflecting the fault state. Therefore, the energy magnitude of each frequency band effectively represents the operational state of the GIS circuit breaker and can be used for fault detection.

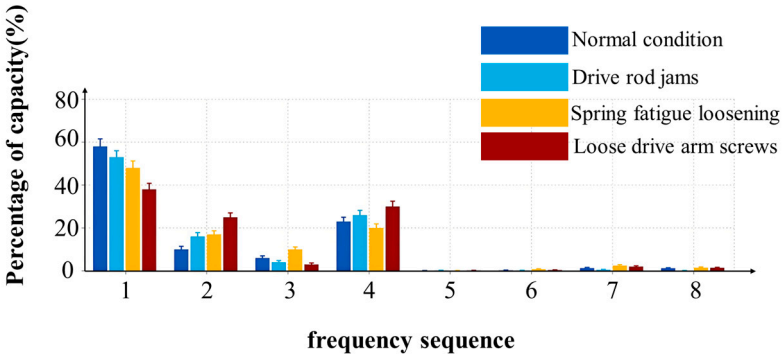


Figure 18. Proportion of energy in each frequency band (%) under different states.

Previous studies have applied rough set theory to process data like circuit breaker current, amplitude, and switching time for fault diagnosis. In this paper, rough set theory is used on the eight parameters from the third layer of wavelet packet decomposition to reduce feature vector dimensionality. Based on the experimental process, 200 data points with clearly defined fault types are extracted, 50 for each type. The initial and minimum decision tables are then established. Because rough set theory works only with discrete data, the first step is to convert the data into discrete form. The energy ratio of eight frequency bands to the total energy for 200 data groups is analyzed. The frequency number is set to three for further analysis. The discretization results are shown in Table 2. The discrete data are then analyzed using rough set theory. The minimum decision table is created by removing redundant conditional attributes based on knowledge approximation, as shown in Table 3.

Table 2. Discretization results.

Causality	Definition	Encoding	Definition	Encoding	Definition	Encoding
T_1	(0.500, 0.650)	0	(0.400, 0.500)	1	(0.300, 0.400)	2
T_2	(0.087, 0.129)	0	(0.130, 0.182)	1	(0.228, 0.273)	2
T_3	(0.050, 0.072)	0	(0.020, 0.035)	1	(0.083, 0.134)	2
T_4	(0.180, 0.238)	0	(0.236, 0.281)	1	(0.295, 0.328)	2
T_5	(0.0005, 0.0010)	0	(0.0004, 0.0006)	1	(0.0002, 0.0005)	2
T_6	(0.0028, 0.0040)	0	(0.0050, 0.0060)	1	(0.0037, 0.0040)	2
T_7	(0.007, 0.028)	0	(0.0032, 0.0080)	1	/	
T_8	(0.0158, 0.3037)	0	/		(0.0083, 0.0187)	2

Table 3. Minimal decision table.

Number	T_1	T_2	T_3	T_4	T_7	Genre
1	0	0	0	0	0	1
2	0	1	2	0	0	1
3	0	1	1	1	1	2
4	1	1	2	0	0	3
5	2	2	1	2	1	4
6	1	0	1	1	1	2
7	0	1	2	1	0	3
8	1	2	1	1	1	4

To apply rough set theory for feature reduction, it is necessary to discretize the continuous wavelet packet energy ratios. In this study, we divided the continuous values into three distinct categories: 0, 1, and 2. The discretization was performed based on the

observed distributions of energy values across the dataset. Specifically, the energy ratios were grouped into the following intervals:

0: Represents the energy ratio range between 0.500 and 0.650. This category captures values that fall within this middle range, which corresponds to moderate energy levels.

1: Represents the energy ratio range between 0.400 and 0.500. This category captures lower energy values, indicating less significant fault activity.

2: Represents the energy ratio range between 0.300 and 0.400. This category captures the lowest energy values, typically associated with very minor or no faults.

The selection of these intervals was based on both empirical observation of the energy distributions and statistical analysis to ensure a reasonable balance between the number of data points in each category. These discretized categories (0, 1, and 2) allow us to simplify the data while preserving its meaningful structure for subsequent analysis using rough set theory.

Each row in Table 2 corresponds to a specific frequency band from the third layer of wavelet packet decomposition, with each value in the row representing the discretization of the energy ratio for that frequency band. This discretization process facilitates the construction of a decision table, which is a critical step in the rough set-based feature reduction. By reducing the dimensionality of the continuous data, we can effectively highlight the most relevant features for fault diagnosis, improving the efficiency and accuracy of the classification process.

The encoded values (0, 1, and 2) in Table 2 were then used to construct a reduced decision table (Table 3), where redundant or irrelevant features are eliminated, and the most significant attributes are retained for further analysis. This transformation enables a more accurate fault classification using the S_Kohonen network and is a key step in ensuring the robustness and reliability of our fault detection methodology.

As shown in Table 2, the initial decision table includes eight conditional attributes and one decision attribute. After reduction, the number of conditional attributes is reduced to five: T_1, T_2, T_3, T_4, and T_7. The decision table after knowledge reduction keeps its simplest form while maintaining valid information. This prepares the basis for the diagnostic process using neural networks.

As shown in Figure 18, the energy proportions of frequency bands 5 and 6 are small and can be ignored. Additionally, there is no significant difference in the energy proportion of frequency band 8 across the four states. Therefore, the feature vector obtained after knowledge reduction using rough set theory, which consists of frequency bands 1, 2, 3, 4, and 7, reflects the actual conditions and can be used as feature parameters, as follows:

$$T = [T_1, T_2, T_3, T_4, T_7] \tag{19}$$

4.3. GIS Circuit Breaker Fault Type Identification Based on the S_Kohonen Network

Previous studies have used BP, RBF, and other neural networks for circuit breaker fault diagnosis. However, these networks are slow to converge and are heavily dependent on sample data. In contrast, the Kohonen network has a simple structure, requires no supervision, and uses fewer sample data [31,32]. It can map high-dimensional data to lower-dimensional spaces while maintaining data integrity. Therefore, the Kohonen network is well suited for fault recognition in GIS circuit breakers.

In this study, the S_Kohonen neural network was trained and evaluated using a total of 400 samples: 280 samples (70 per fault type) for training and 120 samples (30 per fault type) for testing. To ensure that the model was robust and did not overfit to any particular dataset, 5-dimensional cross-validation was applied during training. This approach splits the dataset into five subsets, using each subset as a validation set once, while the remaining subsets are used for training.

The computational cost of training the S_Kohonen network is relatively low compared with more complex deep learning models. The network, with an input layer of five features and a competitive layer of 36 neurons, was trained for 10,000 iterations. Training times were typically on the order of a few minutes to an hour, depending on the size of the dataset and the computational resources available. The proposed method was run on a standard desktop computer with moderate processing power and memory, making it computationally feasible for practical applications.

4.3.1. Kohonen Network

Figure 19 shows the structure of the Kohonen network, which has two layers: the input layer and the neuron layer, with no separate output layer. The neuron layer is arranged in a "plane" structure and is fully connected to the input layer. The weight vector between the input and each neuron matches the input's dimensionality. Through continuous training, the input vector is classified, and the excitation state of each neuron indicates the output.

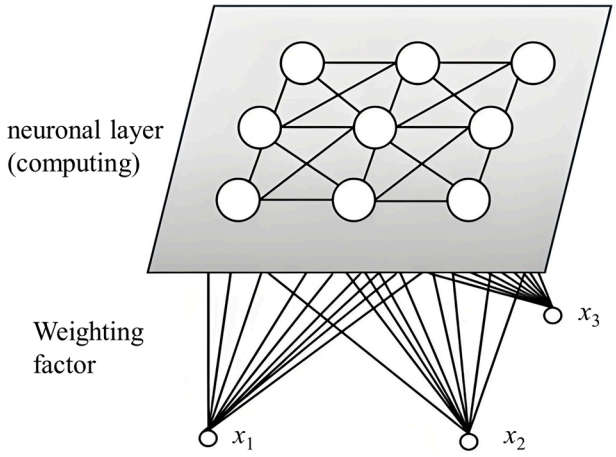


Figure 19. S_Kohonen network structure diagram.

The self-organizing learning process of the Kohonen network: To align the input with the weight vector, it is not necessary to adjust all weights; only a subset needs to be updated. As learning progresses, each weight vector evolves into a pattern that represents its input state. This shows the Kohonen network's ability to perform clustering and automatic recognition.

The training of Kohonen network can be broadly divided into two parts: competition and learning. The steps are as follows:

(1) Competition: For the input vector $X = (x_1, x_2, \cdots, x_n)$, each neuron weight vector w_{ij} is at a distance from it:

$$d_j = \left\| x_i - w_{ij} \right\| \tag{20}$$

In this formula, $j = 1, 2, \cdots, m$. Its minimum value is taken as the winner, i.e.,:

$$j^* = \{ j : \min(d_j) \} \tag{21}$$

(2) Learning: The neurons capable of learning this input pattern are the winning and adjacent neurons filtered by Step (1). Then, the weight coefficients are adjusted:

$$w_{ij} = w_{ij} + \eta (X_i - w_{ij}) \tag{22}$$

η represents the rate of learning, and the size decreases with time. With more and more training, weights will become smaller and smaller, which is the process of weight

adjustment. Based on this, the essential property of the pattern is the weight vector of the victory node connections.

(3) Steps (1) and (2) are repeated, and the training ends when the excitatory neurons correspond stably to the input samples.

After training, the winning node produces the strongest response, followed by its neighboring nodes. The winning node may change as the input state varies. The input patterns and corresponding output node states can be obtained from the Kohonen network's output states.

4.3.2. Improvement of the Kohonen Network

As discussed in the last section, the Kohonen network can classify data states. However, without an output layer, data from the same category may be assigned to different nodes, resulting in multiple classifications. To resolve this, an output layer is added after the competition layer, turning the network into a supervised system, known as the S_Kohonen network.

To align the classification results of the S_Kohonen network with the actual categories, the output layer is set to have the same number of nodes [33]. The weights of the output and competitive layers are adjusted as follows:

$$w_{jk} = w_{jk} + \eta'(Y_k - w_{jk}) \tag{23}$$

In this formula, w_{jk} represents the connection weights between the competing and output layers, η' denotes the learning rate, and Y_k refers to the data sample category.

The addition of the output layer distinguishes the S_Kohonen network from the Kohonen network. When adjusting the weight coefficients, the weights linked to the winning node, both between the input-competition layers and the competition-output layers, must be modified.

4.3.3. Identify GIS Circuit Breaker Fault Types Based on S_Kohonen Networks

The minimum decision table for the transient vibration signals of GIS circuit breaker closing is obtained using wavelet packet rough set knowledge approximation. The feature vector's dimensionality is reduced to five. These five-dimensional feature vectors, normalized for different states, are then input into the improved Kohonen network for fault type identification. The process flow of the S_Kohonen network algorithm is shown in Figure 20.

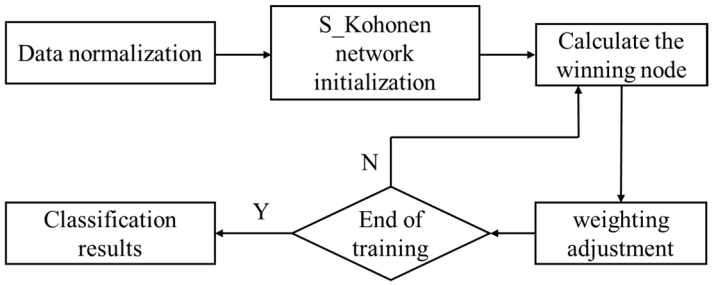


Figure 20. Algorithm flow of the S_Kohonen network.

In this paper, the input feature vector has five dimensions. The intermediate competitive layer contains 36 nodes, which is much larger than the number of input features. The output layer consists of four nodes, corresponding to the actual state categories, and is arranged in a 6 × 6 matrix. This results in a network structure of 5-36-4. The output states represent the following: 1 for normal state, 2 for drive rod jamming, 3 for spring fatigue loosening, and 4 for drive crutch arm screw loosening. A total of 400 feature vectors were

used in the experiment, with 100 samples from each state. These 400 vectors were derived from real data obtained during the simulation. Of these, 280 samples (70 per state) were used for training, and the remaining 120 samples (30 per state) were used for testing. To enhance the recognition accuracy of the S_Kohonen network, training was conducted with randomly selected samples from the training set over 10,000 iterations.

Table 4 shows a subset of the S_Kohonen network's training data. Table 5 presents part of the test data, with each state's data being repeated 30 times. This helps evaluate the network's ability to accurately identify GIS circuit breaker faults.

Table 4. Sample training data for the S_Kohonen network.

Sample Number	Input Feature Vector					Fault Type
	T_1	T_2	T_3	T_4	T_7	
1	0.5770	0.1010	0.0648	0.2290	0.0133	1
2	0.5782	0.1008	0.0657	0.2205	0.0128	1
3	0.5779	0.1012	0.0652	0.2167	0.0118	1
4	0.5679	0.1103	0.0600	0.2212	0.0097	1
5	0.5791	0.1022	0.0583	0.2208	0.0127	1
6	0.5287	0.1559	0.0371	0.2566	0.0058	2
7	0.5183	0.1562	0.0358	0.2479	0.0060	2
8	0.5337	0.1573	0.0342	0.2607	0.0053	2
9	0.5282	0.1683	0.0388	0.2615	0.0067	2
10	0.5290	0.1593	0.0299	0.2483	0.0058	2
11	0.4762	0.1768	0.1021	0.2067	0.0206	3
12	0.4806	0.1752	0.1137	0.2053	0.0211	3
13	0.4796	0.1688	0.1107	0.2006	0.0197	3
14	0.4788	0.1739	0.1203	0.1987	0.0211	3
15	0.4813	0.1683	0.1217	0.1965	0.0203	3
16	0.3793	0.2500	0.0367	0.3062	0.0079	4
17	0.3816	0.2476	0.0285	0.3112	0.0063	4
18	0.3822	0.2387	0.0354	0.2988	0.0070	4
19	0.3765	0.2583	0.0332	0.3108	0.0059	4
20	0.3762	0.2556	0.0296	0.3203	0.0061	4

Table 5. Sample testing data for the S_Kohonen network.

Sample Number	Input Feature Vector					Fault Type
	T_1	T_2	T_3	T_4	T_7	
1	0.5728	0.1263	0.0487	0.2313	0.0108	1
2	0.5652	0.1183	0.0591	0.2301	0.0183	1
3	0.5197	0.1662	0.0289	0.2644	0.0032	2
4	0.5323	0.1587	0.0376	0.2610	0.0007	2
5	0.4693	0.1832	0.1186	0.2002	0.0096	3
6	0.4933	0.1695	0.0988	0.1899	0.0134	3
7	0.3683	0.2700	0.0377	0.3201	0.0016	4
8	0.3725	0.2582	0.0501	0.2903	0.0033	4

The classification results in Figure 21 show that the S_Kohonen network, trained with data from Table 6, accurately identifies the fault types of GIS circuit breakers, confirming its effectiveness. The test results in Table 5 indicate that when the same test data are input multiple times, the network achieves an accuracy of 96.7%, demonstrating its stability. Additionally, the classification categories of the S_Kohonen network align with the actual data, resolving the issue where the Kohonen network could generate more categories than the actual data. Therefore, the S_Kohonen network is effective for mechanical fault

identification in GIS circuit breakers and provides a new method for detecting internal faults in GIS.

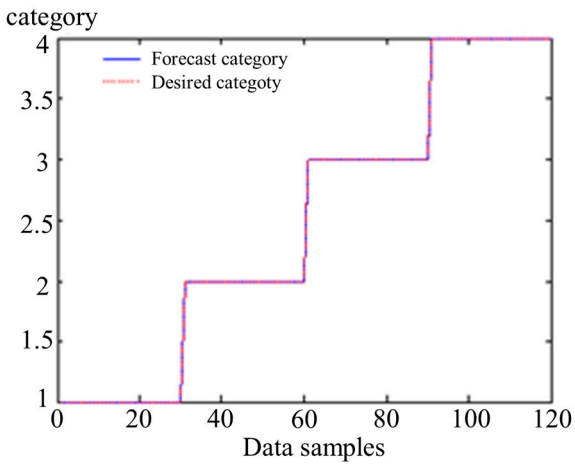


Figure 21. Classification results of the S_Kohonen network.

Table 6. Recognition results of the S_Kohonen network.

Actual Types / Fault Types	Normal Condition	Drive Rod Jams	Spring Fatigue Loosening	Loose Drive Arm Screws
Normal condition	29	1	0	0
Drive rod jams	0	28	0	2
Spring fatigue loosening	1	0	29	0
Loose drive arm screws	0	0	0	30

5. Conclusions

This study investigated a novel fault diagnosis method for GIS circuit breakers based on closing transient vibration signals. By collecting and analyzing the vibration characteristics during the closing process, mechanical faults were effectively identified using wavelet packet transform, rough set theory, and the S_Kohonen neural network.

The main conclusions drawn from this research are as follows:

(1) Vibration Characterization of GIS Circuit Breakers:

Detailed analysis confirms that abnormal mechanical conditions result in significant variations in the transient vibration signals of GIS circuit breakers. These variations serve as reliable indicators for mechanical fault detection.

(2) Feature Extraction and Dimensionality Reduction:

Wavelet packet transform effectively extracts key frequency–domain features from the transient vibration signals, while rough set theory successfully reduces the dimensionality without losing critical fault information. This combination significantly enhances the efficiency of the fault identification process.

(3) Fault Diagnosis Based on the S_Kohonen Network:

The improved Kohonen neural network (S_Kohonen) achieves high accuracy in fault classification. Experimental results indicated a diagnostic accuracy of 96.7%, validating the reliability and robustness of this method within laboratory conditions.

(4) Comparison with Traditional Methods:

Compared with conventional fault detection techniques, the proposed method offers superior accuracy, adaptability, and automation in diagnosing GIS circuit breaker faults, reducing reliance on manual inspections and supporting improved predictive maintenance strategies.

While the current study demonstrates conclusive results in a controlled laboratory environment, it is recognized that further validation using experimental data from various real-world GIS installations would be beneficial. Due to experimental constraints, such validation could not be included in this study. However, future research should focus on collecting and analyzing vibration signals from real operational environments to evaluate and enhance the generalization capability and robustness of the proposed diagnostic method.

Author Contributions: Methodology, Y.Y.; Writing—original draft, Y.Y.; Writing—review & editing, H.Z. All authors have read and agreed to the published version of the manuscript.

Funding: This research was financially supported by the National Key Research and Development Program of China (Grant No. 2023YFB3407703).

Data Availability Statement: The original contributions presented in this study are included in the article. Further inquiries can be directed to the corresponding author.

Conflicts of Interest: The authors declare no conflict of interest.

References

1. Meng, F.; Liu, H.; Wang, J. Research and Analysis on Fault Diagnosis of Gas Insulated Switchgear. In Proceedings of the 2020 12th International Conference on Computational Intelligence and Communication Networks (CICN), Bhimtal, India, 25–26 September 2020; pp. 301–305.
2. Velásquez, R.M.A.; Lara, J.V.M. Root cause analysis methodology for circuit breaker associated to GIS. *Eng. Fail. Anal.* **2020**, *115*, 104680. [CrossRef]
3. Dolkun, D.; Gong, D.; Du, J.; Zhan, Z. Analysis of an electric breakdown fault of circuit breaker in 220 kV GIS equipment. In Proceedings of the 2021 3rd International Academic Exchange Conference on Science and Technology Innovation (IAECST), Guangzhou, China, 10–12 December 2021; pp. 1644–1647.
4. Liu, S.; Liu, J.; Wang, X. An analysis method of GIS equipment fault causes based on online monitoring and joint diagnosis. In Proceedings of the 2022 IEEE 4th International Conference on Power, Intelligent Computing and Systems (ICPICS), Shenyang, China, 29–31 July 2022; pp. 98–101.
5. Zhou, D.; Ren, A.; He, Y.; Liu, F.; Yao, X.; Xue, Z.; Zhang, J. Defect detection technology of gas insulated switchgear based on ultra-high frequency method and ultrasonic method after earthquake. In Proceedings of the 13th International Conference on Quality, Reliability, Risk, Maintenance, and Safety Engineering (QR2MSE 2023), Kunming, China, 26–29 July 2023; pp. 408–413.
6. He, L.; Yang, J.; Zhang, Z.; Li, Z.; Ding, D.; Yuan, M.; Li, R.; Chen, M. Research on mechanical defect detection and diagnosis method for GIS equipment based on vibration signal. *Energies* **2021**, *14*, 5507. [CrossRef]
7. Zhong, Y.; Hao, J.; Ding, Y.; Liao, R.; Xu, H.; Li, X. Novel GIS mechanical defect simulation and detection method based on large current excitation with variable frequency. *IEEE Trans. Instrum. Meas.* **2022**, *71*, 1–15. [CrossRef]
8. Xiping, J.; Huadong, P.; Jie, L.; Yingkai, L.; Wei, Q.; Yao, Z.; Jian, H. Operation GIS Equipment Mechanical Vibration Law and Defect Development Trend Analysis. In Proceedings of the 2023 IEEE International Conference on Power Science and Technology (ICPST), Kunming, China, 5–7 May 2023; pp. 199–202.
9. Honggang, C.; Mingyue, X.; Chenzhao, F.; Renjie, S.; Zhe, L. Mechanical fault diagnosis of GIS based on MFCCs of sound signals. In Proceedings of the 2020 5th Asia Conference on Power and Electrical Engineering (ACPEE), Chengdu, China, 4–7 June 2020; pp. 1487–1491.
10. Zhao, J.; Xiong, Q.; Zhang, C.; Guo, Z.; Zhu, L.; Liang, Z.; Tian, J.; Chen, S. Mechanical State Detection of GIS Circuit BreakerBased on Vibration Characteristics. In Proceedings of the 2020 8th international conference on condition monitoring and diagnosis (CMD), Phuket, Thailand, 25–28 October 2020; pp. 166–169.
11. Zhong, Y.; Gong, R.L.; Su, S.; Hao, J.; Wang, Q.; Jiang, X. Identification method of abnormal contact defect on GIS conductor base and disconnector contact based on ensemble empirical mode decomposition. In Proceedings of the 2020 8th International Conference on Condition Monitoring and Diagnosis (CMD), Phuket, Thailand, 25–28 October 2020; pp. 118–121.
12. Baiquan, C.; Bangfa, C.; Pengyang, W.; Xuan, G.; Qiang, L. Research on electrical contact fault characteristics of GIS circuit breaker based on vibration signal. In Proceedings of the 2021 Annual Meeting of CSEE Study Committee of HVDC and Power Electronics (HVDC 2021), Hybrid Conference, 28–30 December 2021; pp. 110–115.
13. Ma, Z.; Liu, B.; Tang, R. GIS mechanical fault diagnosis and test analysis based on S transform-SVM-AlexNet model. In Proceedings of the 2020 12th IEEE PES Asia-Pacific Power and Energy Engineering Conference (APPEEC), Nanjing, China, 20–23 September 2020; pp. 1–5.

14. Qu, B.; Wang, Y.; Zhou, L.; Wang, K.; Wang, Z.; Wang, J.; Chen, H. GIS vibration test method and characteristic signal recognition. *Proc. J. Phys. Conf. Ser.* **2021**, *1865*, 032021. [CrossRef]
15. Zhao, W.; Wen, F.; Wu, S.; Chu, Z.; Sheng, Z.; Ji, K. Fault diagnosis of GIS disconnector based on BP neural network. In Proceedings of the 2021 13th International Symposium on Linear Drives for Industry Applications (LDIA), Wuhan, China, 1–3 July 2021; pp. 1–5.
16. Ding, R.; Zhao, K.; Teng, Y.; Zhuang, T.; Liu, J.; Yang, J. Detection and analysis of GIS discharge defects based on deep learninng method. In Proceedings of the 2022 4th Asia Energy and Electrical Engineering Symposium (AEEES), Chengdu, China, 25–28 March 2022; pp. 706–711.
17. Jiuye, Z.; Yubo, Z.; Haoli, L.; Jing, X.; Shaoqing, P.; Liang, W. Research on key technologies of digital sensing and fault warning of isolation switch in GIS. *Proc. J. Phys. Conf. Ser.* **2024**, *2806*, 012007. [CrossRef]
18. Yongxiang, L.; Ming, Z.; Jie, M.; Yongka, Q.; Kejian, Z.; Ming, F.; Dexin, N.; Zhixiang, L. Gas-insulated switchgear (GIS) equipment mechanical fault detection based on feature learning of vibration signal images. In Proceedings of the 2021 International Conference on Advanced Electrical Equipment and Reliable Operation (AEERO), Beijing, China, 15–17 October 2021; pp. 1–4.
19. Alsumaidaee, Y.A.M.; Yaw, C.T.; Koh, S.P.; Tiong, S.K.; Chen, C.P.; Ali, K. Review of medium-voltage switchgear fault detection in a condition-based monitoring system by using deep learning. *Energies* **2022**, *15*, 6762. [CrossRef]
20. Jiang, Y.; Xu, M.; Lin, R.; Hong, L.; Lu, G.; Li, Z. GIS mechanical fault diagnosis method based on middle time Mel cepstrum coefficient. *Proc. J. Phys. Conf. Ser.* **2020**, *1659*, 012055. [CrossRef]
21. Zheng, X.; Li, J.; Yang, Q.; Li, C.; Kuang, S. Prediction method of mechanical state of high-voltage circuit breakers based on LSTM-SVM. *Electr. Power Syst. Res.* **2023**, *218*, 109224. [CrossRef]
22. Wu, H.; Zhang, J.; Wang, J.; Sun, Y.; Tan, R.; Sun, D.; Zhang, N. GIS Fault Diagnosis Method Based on Multi-Source Feature Dual Decision Hybrid Classification Network. In Proceedings of the 2024 9th Asia Conference on Power and Electrical Engineering (ACPEE), Shanghai, China, 11–13 April 2024; pp. 2077–2082.
23. Sang, Z.; Gu, X.; Wang, Y.; Jiang, W.; Cheng, W. Waveform Correlation Analysis Method for Mechanical Characteristics of Circuit Breaker in Intelligent GIS Equipment. *Proc. J. Phys. Conf. Ser.* **2022**, *2218*, 012054. [CrossRef]
24. Zhang, J.; Zhao, Y.; Liu, H.; Xu, J.; Peng, S.; Wang, L. Research on fault diagnosis method of GIS isolation switch. In Proceedings of the 2024 3rd International Conference on Energy, Power and Electrical Technology (ICEPET), Chengdu, China, 17–19 May 2024; pp. 1507–1510.
25. Ma, H.; Liu, B.; Xu, H.; Chen, B.; Ju, P.; Zhang, L.; Qu, B. GIS mechanical state identification and defect diagnosis technology based on self-excited vibration of assembled circuit breaker. *IET Sci. Meas. Technol.* **2020**, *14*, 56–63. [CrossRef]
26. Xu, Y.; Wang, L. Fault diagnosis system based on rough set theory and support vector machine. In Proceedings of the International Conference on Fuzzy Systems and Knowledge Discovery, Changsha, China, 27–29 August 2005; pp. 980–988.
27. Sánchez, R.-V.; Macancela, J.C.; Ortega, L.-R.; Cabrera, D.; García Márquez, F.P.; Cerrada, M. Evaluation of hand-crafted feature extraction for fault diagnosis in rotating machinery: A survey. *Sensors* **2024**, *24*, 5400. [CrossRef] [PubMed]
28. Huang, L.; Huang, H.; Liu, Y. A Fault Diagnosis Approach for Rolling Bearing Based on Wavelet Packet Decomposition and GMM-HMM. *Int. J. Acoust. Vib.* **2019**, *24*, 199–209. [CrossRef]
29. Li, C.; Sánchez, R.-V.; Zurita, G.; Cerrada, M.; Cabrera, D. Fault diagnosis for rotating machinery using vibration measurement deep statistical feature learning. *Sensors* **2016**, *16*, 895. [CrossRef] [PubMed]
30. Li, Y.; Ning, F.; Jiang, X.; Yi, Y. Feature extraction of ship radiation signals based on wavelet packet decomposition and energy entropy. *Math. Probl. Eng.* **2022**, *2022*, 8092706. [CrossRef]
31. Bay, O. Kohonen network based fault diagnosis and condition monitoring of pre-engaged starter motors. *Int. J. Automot. Technol.* **2005**, *6*, 341–350.
32. Chowdhury, B.H.; Wang, K. Fault classification using Kohonen feature mapping. In Proceedings of the International Conference on Intelligent System Application to Power Systems, Orlando, FL, USA, 28 January–2 February 1996; pp. 194–198.
33. Wu, G.-n.; Xu, C.; Du, F.; Zhu, W.-d. A modified time reversal method for guided wave detection of bolt loosening in simulated thermal protection system panels. *Complexity* **2018**, *2018*, 8210817. [CrossRef]

Disclaimer/Publisher's Note: The statements, opinions and data contained in all publications are solely those of the individual author(s) and contributor(s) and not of MDPI and/or the editor(s). MDPI and/or the editor(s) disclaim responsibility for any injury to people or property resulting from any ideas, methods, instructions or products referred to in the content.